2017

Gradient in microstructure and mechanical property of selective laser melted AlSi10Mg

Yujing Liu
Edith Cowan University

Zeng Qian Liu

Y Jiang

G.W Wang

Yang Yang

See next page for additional authors

10.1016/j.jallcom.2017.11.020
Liu, Y. J., Liu, Z., Jiang, Y., Wang, G. W., Yang, Y., & Zhang, L. C. (2018). Gradient in microstructure and mechanical property of selective laser melted AlSi10Mg. *Journal of Alloys and Compounds, 735*, 1414-1421. Available here

Accepted Manuscript

Gradient in microstructure and mechanical property of selective laser melted AlSi10Mg

Y.J. Liu, Z. Liu, Y. Jiang, G.W. Wang, Y. Yang, L.C. Zhang

PII: S0925-8388(17)33766-0

DOI: 10.1016/j.jallcom.2017.11.020

Reference: JALCOM 43713

To appear in: *Journal of Alloys and Compounds*

Received Date: 25 August 2017

Revised Date: 2 November 2017

Accepted Date: 3 November 2017

Please cite this article as: Y.J. Liu, Z. Liu, Y. Jiang, G.W. Wang, Y. Yang, L.C. Zhang, Gradient in microstructure and mechanical property of selective laser melted AlSi10Mg, *Journal of Alloys and Compounds* (2017), doi: 10.1016/j.jallcom.2017.11.020.

Gradient in microstructure and mechanical property of selective laser melted AlSi10Mg

Y.J. Liu[a] , Z. Liu[b] , Y. Jiang[b], G.W. Wang[b], Y. Yang[c,d,*], L.C. Zhang[a,**]

[a]*School of Engineering, Edith Cowan University, 270 Joondalup Drive, Joondalup, Perth, WA 6027, Australia*

[b]*Shenyang National Laboratory for Materials Science, Institute of Metal Research, Chinese Academy of Sciences, 72 Wenhua Road, Shenyang 110016, China*

[c]*Key Laboratory of Optoelectronic Materials Chemistry and Physics, Fujian Institute of Research on the Structure of Matter, Chinese Academy of Science, Fuzhou 350002, China*

[d]*Shenzhen Key Laboratory of Human Tissue Regeneration and Repair, Shenzhen Institute, Peking University, Shenzhen 518057, China*

ABSTRACT

It is known that metal parts can be made stronger, tougher and better wear resistance by introducing gradient microstructure. This work reports the cooling rate of melt pool induced discrepancy in microstructural gradient and element distribution during selective laser melting (SLM), therefore resulting in decrease in microhardness and wear resistance from surface to inside with a range of ~100 μm of SLM-manufactured AlSi10Mg alloy. The cooling rate in the top surface of melt pool reaches ~1.44×10^6 K/s, which is much higher than that at the bottom ($\leq1\times10^3$ K/s). Such a difference in cooling rate of melt pool is the main cause for forming gradient

* Corresponding author. E-mail address: yy@fjirsm.ac.cn (Y. Yang)
** Corresponding author. E-mail addresses: lczhangimr@gmail.com, l.zhang@ecu.edu.au (L. C. Zhang).

microstructure in terms of the distribution of Si particles, dendrite size, sub-grains and sub-boundaries. The variation in microstructure of SLM-produced AlSi10Mg alloy, as a result of gradient cooling rate, has a significant impact on its mechanical properties. Compared with core area, the surface area with a higher cooling rate is composed of finer Si particles, dendritic structure and more sub-boundaries, resulting in higher microhardness and greater wear resistance. The mechanism for formation of gradient microstructure and its influence on the mechanical properties are discussed, which provide new and deep insight into fabricating SLM-produced components with gradient microstructure.

Keywords: Selective laser melting; Gradient microstructure; Mechanical properties; AlSi10Mg; EBSD

1. Introduction

The increasing demand for metal parts with complex shapes and high qualities has motivated the development of advanced manufacturing technologies. Selective laser melting (SLM), as one of common metallic additive manufacturing technologies, has been well known with capability to create high-quality and defect-free complex components [1]. So far, a number of SLM-fabricated alloys, such as steels, titanium alloys and aluminum alloys, have been reported to exhibit excellent mechanical properties [2-5] and comparable corrosion resistance compared to their counterparts manufactured by traditional technologies.

As one of the largest industrial usage of aluminum alloy, Al-Si alloys have numerous advantages including light weight, good wear resistance, good thermal expansion coefficient, high specific strength and good thermal conductivity, thereby making them widely used in automobile and aerospace industries [6]. It is well known that the mechanical properties are sensitive to the microstructure including the phase constituents, grain size and morphologies, dendrite and elemental segregation [7, 8]. Therefore, manipulation and optimization of microstructure is a widely known strategy to achieve satisfactory mechanical properties for industrial applications. Considerable efforts have been made to manipulate microstructural features including dendrite size, grain size and morphologies, subgrains and boundaries to enhance mechanical properties [8]. Among the strategies, grain refinement is most widely used to strengthen metal parts [9]. Usually, grain refinement is realized by plastic deformation techniques such as rolling, drawing, forging and equal channel angular pressing (ECAP) [8, 10]. Furthermore, the formation of, and interactions among, sub-boundaries or internal dislocations are commonly found in the process of grain refinement [11]. The dislocations and sub-grain boundaries resulting from plastic deformation play a significant role in improving the hardness and strength of a material [10]. However, conventional plastic deformation methods are hard to manufacture metal parts with complex geometries. Fortunately, SLM has capability of producing complex parts with fine microstructure as a result of fast cooling rate during SLM process, which was reported to reach a magnitude order of 10^7 K/s during solidification in SLM process [12, 13]. Theoretically, the dendrites formed

during solidification process in SLM and their size, strongly relying on the cooling rate in SLM process, play a decisive role in the final properties of SLM-produced components [14, 15]. It has now well been acknowledged that fast cooling rate in SLM process can refine the microstructure in terms of grain size, secondary dendrite arm spacing (SDAS) size, age-hardenable Mg/Si precipitates [16, 17]. Li *et al.* [14] found that cooling rate played a critical role in SLM process, which resulted in ultrafine-grained eutectic microstructure in the as-produced AlSi10Mg samples. Such a unique microstructure significantly enhanced the tensile properties and Vickers microhardness. Moreover, the microstructure is sensitive to the laser melting process. Anwar *et al*. [18] revealed that the laser scan direction and the gas flow velocity could affect the microstructure therefore the tensile properties due to the interaction of laser-spattered and powder-gas, thereby resulting in input energy loss. Rao *et al.* [19] found that the Si particles combined with tensile properties could be affected by the melt pool and building direction. Kimura *et al.* [20] found that the microstructure of the as-produced SLM samples comprised of sub-micron fine dendrite with an elongated shape in the direction of stacking. Furthermore, the gradient thermal distribution has been found in SLM process due to different cooling rate [21]. Such gradient thermal distribution would influence the solidification process of the powder in SLM process, thereby inducing the formation of gradient microstructure in the SLM-produced components. Gradient microstructure in a structure of increasing grain size from surface to inside is confirmed to play a positive role in improving mechanical properties [22].

In addition, the mechanical property of Al–Si alloys could be significantly affected by the size and distribution of the eutectic silicon (Si) in microstructure. For example, McDonald *et al.* [23] pointed out that the Al-Si parts with large acicular silicon particles have poor fatigue properties as a result of low ductility. Delahaye *et al.* [24] found that the refinement of the Si particles in Al-Si alloy is regarded as the most important factor for optimizing its mechanical properties. With the aim to satisfy the high standard requirements of industry, considerable endeavors have been made to improve the mechanical properties by manipulating the eutectic microstructure in Al-Si alloys [15, 25]. In general, two main methods are often used to refine grains, i.e. suitable microalloying and increasing cooling rate during solidification [6]. Addition of new elements can promote refining Si particles. However, it was reported the addition of new elements might reduce the metal fluidity thereby increasing the cost for producing a part. Furthermore, the main drawback is that the alloying elements are rapidly lost in the alloy due to evaporation or oxidation [26]. Differently, rapid solidification can reduce even avoid these above disadvantages to improve mechanical properties. Studies on the high cooling rate of Al-Si alloys have shown that the solid solubility of Si particles in Al matrix can be remarkably increased under a high cooling rate [27].

AlSi10Mg, which is one of the Al-Si alloys, has been widely studied and manufactured by SLM [15, 16, 24, 28]. Thanks to the high cooling rate in SLM process, SLM-produced Al-Si components exhibit enhanced mechanical properties compared to their counterparts manufactured by traditional technologies. However,

the solidification process of SLM is very complex and the cooling rates at different positions of melt pool in SLM are different and difficult to detect. As such, the effect of the SLM solidification with different cooling rate on the resultant microstructure therefore properties is still unknown.

As such, in this work, the AlSi10Mg alloy was selected to study the effect of the cooling rate in the melt pool on the formation of gradient microstructure and the resultant mechanical properties. The cooling rate of melt pool in SLM was calculated by finite element modeling (FEM). The Si particle size and distribution, sub-boundaries and dendrites were compared and analyzed.

2. Experimental

The nominal chemical composition of the gas-atomized AlSi10Mg powder used in this work was analyzed to be 9.3Si, 0.4Fe, 0.05Cu, 0.1Mu, 0.3Mg, 0.1Zn, 0.05Ni, 0.1Cr, and Al balance (wt. %). The size of spherical powder ranges from 15 μm to 55 μm and with a Gaussian distribution centered on 35 μm (Fig. 1a). Cubic samples with dimensions of 10 ×10 ×10 mm^3 was manufactured by using a BLT-S300 SLM machine (Xi'an Bright Additive Technologies Co., Ltd) with the following processing parameters: input of laser power of 500 W, laser scan speed of 1500 mm/s and layer thickness of 30 μm. The zigzag pattern was used as the scanning strategy to decrease the thermal stress between layers, while the scanning angle was alternated by 90° upon the precedent layer. In order to compare the microstructural feature and physical properties of surface and core regions, two groups of samples were cut at 50 μm and

200 μm in depth below the top surface (hereafter denoted as Sample-A and Sample-B respectively) for further microstructural characterization and property evaluation. The sample information is shown in Fig. 1b.

Phase identification of the specimens was conducted with an X-ray diffractometer (XRD; D/Max-2500PC) from 20 to 90° with a step size of 0.02°. The microstructural characterization and chemical composition were conducted on Olympus PMG-3 Optical microscope (OM) and JSM-6301F field emission scanning electron microscope (SEM) equipped with energy dispersive spectroscopy (EDS). SEM-based electron back scatter diffraction (EBSD) analyses were carried out in the SEM mentioned before equipped with an Aztec EBSD system with a step size of 0.5 μm. The samples for OM and SEM microstructural observations were etched by a reagent composed of 3% HF, 10% HNO_3, and 87% H_2O (vol. %) for 20 s. However, the EBSD samples were produced only by grinding and electrolytic polishing without etching. In order to investigate the influence of cooling rate on the SLM-produced microstructure, only XZ section (along the build direction) of the samples was characterized. Vickers micro-hardness tests were carried out using a Future Tech Fm-700 machine at a 50g load, whereas all the hardness data shown were averaged from minimal ten parallel testing values.

Finite element modeling (FEM) was performed by Comsol 4.2a software. The dynamic temperature field in the specimen was simulated using the heat transfer module in the FEM. The FEM geometry was cubic with a size of 10 ×10 ×10 mm^3. The same processing parameters, such as the scan speed of 1500 mm/s and layer

thickness of 30 μm, were used as in SLM process. The top surface condition was set as the argon gas atmosphere with a room temperature. The temperature data of the monitoring points at different times can be obtained, then the temperature was used to derive the heating rate and the cooling rate.

In order to evaluate the effect of cooling rate on wear properties, specimens with the gauge of 3 mm in diameter and 5mm in height were cut on the top surface and deep inward, respectively. The MMW-1A machine, which comprised three cylinder against a plate sliding system, was used for wear testing. The cylinder specimens had a round contact surface with a stainless steel plate. The test parameters were set as load of 80 N and speed of 200 r/min at a room temperature. Three samples were tested and the test lasted 1 hour with a step of 15 min; the weights of specimens were measured for each step and the wear weights were calculated subsequently.

3. Results

The XRD patterns of the SLM as-built specimens are shown in Fig. 2. The Si particle (Fd3m, fcc, a=0.5429nm) and α-Al phase (Fd3m, fcc, a=0.4049nm) are identified on the profiles. Usually, the crystallinity degree can be reflected from the peak width of XRD pattern; a wider peak means lower crystallinity degree. As such, the group A has a lower degree of crystallinity with a wider peak of Al matrix than the group B. Fig. 3 shows the EBSD mapping results of the sample A and B in the X-Z cross-section along the Z-direction based on crystallographic parameters of the α-Al phase identified by XRD profile. The reason why Si phase was not considered for

diffraction is that its small size in nanometer is less than the detecting resolution of the machine. Figs. 3a and 3c present the image quality mapping (IQ) results, while Figs. 3b and 3d show the inverse pole figure mapping of the Z-direction (IPF-Z). As can be seen, the α-Al grains in Sample-A near the top surface show a random crystallographic orientation. By contrast, the grains far away from the top surface are elongated and exhibit a strong texture aligned along the <100>//Z direction due to homoepitaxial growth. Such strongly textured grains, presenting a cubic fiber, have been extensively reported in different alloying systems and are attributed to thermal dissipation gradient [2, 3, 29].

From the IPF mapping, special areas with fine and equiaxed grains can be observed along a curving area which has the exact feature of the melting pool. This phenomenon is caused by the heterogeneous nucleation occurring in front of the liquid-solid interface and is similar to the chill zone in the cast process [30]. Taking the misorientation of grain boundaries (GB) into consideration, the misorientation values higher than 10^{o} are outlined by black lines and those lower than 10^{o} are marked by with red lines. Indeed, the area near the top surface within a depth of ~100 μm in Sample-A consists of not only the equiaxed grains with higher misorientation, but also a high density of low-angle subgrain boundaries with red lines and enlarged in Fig. 3b. Such low-angle subgrain boundaries composed of dislocation tangles can be linked to the thermal stress due to fast cooling and lack of sufficient thermal cycling compared to the elongated grains below in which the subgrain boundaries are rarely observed [8, 11]. Such a phenomenon could be analyzed to link with the improved mechanical

properties in terms of the microhardness and strength.

Fig. 4 shows the microstructural morphology and EDS mapping in the X-Z cross-section. To be detailed, the Figs. 4a and b correspond to that of Sample-A, while Figs. 4c and d are related to Sample-B. The dendritic morphologies can be observed in both two samples which show a similar dendrite of α-Al phase and interdentritic Si-particles as reported in literature [28, 31, 32]. It is worth noting that the dendrite size between the two samples is different. The Sample-A near the top surface exhibits near equiaxed fine dendrites with a smaller size of 500 nm (Fig. 4a) and Si particles with a size of less than 50 nm (Fig. 4b), while the Sample-B shows elongated and coarse dendrites sized exceeding 2 μm (Fig. 4c). Furthermore, the distribution of Si (highlighted in red color in Figs. 4b and d) should also be noted. The element of Si distributes relatively uniformly in Sample-A with no noticeable segregation. However, the Si-particles shows an obvious tendency of interdendritic segregation in Sample-B. The observed EDS results are thus consistent with the phase diagram that the Si particles precipitate on the fast cooling condition due to its limited solubility (approximately 0.05%) in Al-based alloy.

Fig. 5 shows the variation of cooling rate around the melt pool boundary. It has been reported that the heat transfer in melt pool depends on the dynamic movements of the metallic liquids including turbulence and convection [33]. The melt pool boundaries are regarded as solid-liquid interfaces and the beginning of solidification, so the study on cooling rate of the melt pool boundaries can help understand the reasons for the formation of microstructure gradient. It is clearly that the cooling rate of the top melt

pool boundary is different from that of the bottom. The cooling rate of the upper surface even reaches 1.44×10^6 K/s, which is much higher than that of the bottom cooling rate with $\leq 1\times 10^3$ K/s. Such a high gradient in cooling rate would affect the microstructure formed in SLM-produced AlSi10Mg components, including sizes of dendrite and the Si-particle. The specific reason is that Si particles in the metal matrix cannot be precipitated and evenly distribute in the matrix, thereby forming a fine microstructure with uniform grains [34].

Fig. 6 illustrates the morphology of indentations of Vickers hardness measurements at the XZ cross-section, the tested points are along z direction from the surface to bottom and the distance is ~50 μm near the top. Notably, with the increase in the distance from the top surface, the indentation size significantly increases. This demonstrates that the hardness value decreases from the top area to bottom. The hardness value of the top area (sample A) is 148±7 HV (Fig. 7), then it drops to 126±6 HV dramatically with a distance of only 50 μm at the position 2. Such a significant difference is caused by the Si particle size and distribution. The Si particles in the bottom area are large and mainly distribute at the interdentritic. Differently, the size of the Si particles is small and evenly distributes in the dendrite. These fine Si particles contributes to increase in hardness values.

Fig. 8a shows the relationship between the wear amount of AlSi10Mg alloy and time for both sample A and B. It is clearly that the wear weight rate of sample A is less than that of sample B. However, these two groups possess a similar coefficient of friction (COF) (Fig. 8b). Undoubtedly, the finer Si particles and the sub-boundaries would

enhance the wear resistance property. The same trend has been found in the results of hardness and wear resistance property: the wear resistance increases with an increase in hardness of the material. For such a case, the acknowledgement of wear property implies that the wear resistance ability is directly proportional to the hardness of the material: a higher hardness will improve the wear resistance property [35]. Based on the results of Fig. 8b, the finer Si particles has a little effect on the coefficient of friction. This could be attributed to the similar contents of Si element in two samples, resulting in limited influence on the coefficient of friction of the two samples.

4. Discussion

4.1 Relationship between microstructure and cooling rates

The cooling rate is one of the dominating factors during solidification process to determine the final properties of metal parts [36-39]. On one hand, fast cooling rate in the SLM solidification process leads to formation of unique microstructure [40]. For example, the displacive martensitic phase with extremely fine size was found in SLM Ti-6Al-4V samples due to fast cooling rate which was responsible for the improvement of the tensile strength [41]. The high cooling rate can even reach to the extent that the metallic glass parts can be produced by SLM. Pauly *et al.* [42] pointed out that the SLM process with layer-wise construction manner is suitable for manufacturing bulk metallic glass parts due to a fast processing cooling rate. Furthermore, the diffusion rate of metal atoms and alloying elements is limited due to fast cooling rate [6, 43]. Prashanth *et al.* [43] found that the Al and Si distribution in

SLM-produced parts are not uniform; Si particles concentrate at the boundaries of lamellae with a size of 200 nm. As the cooling rate can affect the degree of crystallinity, the SLM-produced samples exhibit a lower degree of crystallinity compared with the cast counterparts [43]. In addition, Al-Bermani *et al.* [44] showed that the formation of subgrains and low grain boundaries (sub-boundaries) are evident in columnar primary β grains under a fast cooling. The AM-produced products are slightly different from conventional parts with regard to microstructure and properties. Hence, it is necessary to analyze the specific solidification process for a typical metal material during SLM manufacturing.

The metal powder would quickly melt into a liquid pool once the high-energy laser scans on it, thereby promoting the distribution of alloying elements. As such, rapid cooling inhibits the growth of grains and alloying elements segregation. This leads to that the metal matrix in the solid solution of the alloying elements cannot be precipitated and are evenly distributed in the matrix, thereby refining grains to form fine microstructure. It is know that the size and shape of melt pool are determined by the input laser energy and laser scan speed [45]. Even for a given melt pool, the cooling rates of the top area and of the bottom area are quite different. Liu *et al.* [40] had pointed that the cooling rate has a significant influence on the microstructure and the dendritic growth (therefore the size of dendrites). Thus, it is necessary to study the relationship of the cooling rate and microstructure including the dendritic size and Si particles in the Al matrix.

Due to the small size of the melt pool, nowadays it is impossible to obtain the real

temperature by *in situ* monitoring techniques. However, FEM can be adopted to simulate the size and shape of melt pool as well as the thermal field distribution. The cooling rate can be calculated based on the temperature variation [46].

Interestingly, the cooling rate has important influence on dendrite arm spacing size. Stefanescu [47] has revealed the relationship of the dendrite arm size (λ_1) and the cooling rate *T*,

$$\lambda_1 = \mathrm{c}_t \cdot T^{-n} \quad (1)$$

where c_t is the constant of AlSi10Mg alloy and *n* is the rate exponent. This equation indicates that the dendrite size decreases with increasing the cooling rate. Hence, the difference in dendrite size between sample A and B can be easily explained based on the above results. Additionally, sub-boundary formation can be affected by the fast cooling rate. Hirsch *et al.* [48] reported polycrystalline aluminum sample containing many dislocation loops after quenched from ~600 °C into iced brine. Theoretically, the dislocation loops have the same formation mechanism with sub-boundary. So, it can infer that the sub-boundaries near the top surface are caused by the fast cooling rate.

4.2 The mechanical properties of gradient microstructure

The mechanical properties of Al-Si alloys are significantly determined by the microstructure structure in terms of distribution of eutectic Si in Al matrix, subgrains and sub-boundaries [9-11, 14, 22, 26]. Mechanical properties of metal parts vary significantly with the microstructure including the phase type, grain size and shape,

dendrite and element segregation [7, 8]. It continues to be a major scientific challenge to optimize microstructure. It is well accepted that plastic deformation methods including rolling, drawing forging and ECAP can promote grain refinement [8-11]. Accordingly, the sub-boundaries or internal dislocations could be found in the process of plastic deformation process [11]. The generation of the dislocations and sub-grain boundaries can strengthen the hardness and strength [10]. The wear resistance of the material is determined by its hardness. Ma et al. [49] had revealed that the finer particle size and higher hardness in aluminum alloy composites could increase wear resistance.

In cast Al-Si alloy, there are usually a large number of needle-like or plate-like eutectic Si and even coarse primary Si particles [6]. Such Si particles would significantly fragment the Al matrix, thereby deteriorating the mechanical properties of Al-Si alloy (especially the toughness). Significant decrease in the toughness would be unfavorable for the machinery performance of Al-Si alloy. As such, extensive endeavors have been made to study the eutectic Si and primary Si refinement to improve the mechanical properties of Al-Si alloy. Conventionally, the metamorphic treatment is usually used for Al-Si alloy to suppress the growth of Si phase. After microstructure manipulation, the Si grains in the Al-Si alloy are small, which result in remarkable enhancement in the strength and toughness of the Al-Si alloy [50]. Usually, the addition of alkali metal elements and rare earth elements to the modified Al-Si alloy can be modified to a certain extent, to suppress the growth of Si phase in Al-Si alloy, to refine the grains and improve the mechanical properties. However, such a

method could reduce the flowability property of Al-Si alloy, thereby affecting its casting performance.

5. Conclusions

In this work, the relationship of AlSi10Mg alloy microstructure and the cooling rate based on selective laser melting (SLM) technology is systematically studied and analyzed. Based on these experiments, the results are summarized as follows.

1. The cooling rate of the area near the top surface of the AlSi10Mg SLM-produced specimen reached 1.44×10^6 K/s, which is much higher than that of bottom with $\leq 1\times 10^3$ K/s.
2. Microstructure and mechanical properties show a significant gradient performance with a range of ~100 μm. The top surface area has a lower degree of crystallinity of Al matrix than that of core area.
3. Compared with the bottom area of melt pool with a lower cooling rate, a higher cooling rate in the top area can lead to formation of subgrains and sub-boundaries, as well as the finer Si particles. Such microstructural features usually exist in the solid solution of the alloying and cannot be precipitated and evenly distributed in the AlSi10Mg matrix, resulting in finer dendritic structure.
4. The surface area obtains a higher hardness and greater value wear resistance due to the finer Si particles evenly distributed, finer dendrites and occurrence of sub-boundaries compared with the core area.

Acknowledgement

This work was supported by Shenzhen Fundamental Research (JCYJ 20160427170611414), Australian Research Council Discovery Project (DP110101653). Y.J. Liu is grateful for the financial support from ECU-PRS (International) Scholarship Scheme.

References

[1] Y. Liu, S. Li, W. Hou, S. Wang, Y. Hao, R. Yang, T. B. Sercombe, L.-C. Zhang, Electron Beam Melted Beta-type Ti–24Nb–4Zr–8Sn Porous Structures With High Strength-to-Modulus Ratio, J. Mater. Sci. Technol. 32 (2016) 505-508.
[2] Y. Liu, H. Wang, S. Li, S. Wang, W. Wang, W. Hou, Y. Hao, R. Yang, L.-C. Zhang, Compressive and fatigue behavior of beta-type titanium porous structures fabricated by electron beam melting, Acta Mater. 126 (2017) 58-66.
[3] L. Thijs, K. Kempen, J.-P. Kruth, J. Van Humbeeck, Fine-structured aluminium products with controllable texture by selective laser melting of pre-alloyed AlSi10Mg powder, Acta Mater. 61 (2013) 1809-1819.
[4] T. Sercombe, X. Li, Selective laser melting of aluminium and aluminium metal matrix composites: review, Mater. Technol. 31 (2016) 77-85.
[5] X. Li, C. Kang, H. Huang, L.-C. Zhang, T. B. Sercombe, Selective laser melting of an Al 86 Ni 6 Y 4.5 Co 2 La 1.5 metallic glass: Processing, microstructure evolution and mechanical properties, Mater. Sci. Eng. A 606 (2014) 370-379.
[6] X. Li, X. Wang, M. Saunders, A. Suvorova, L.-C. Zhang, Y. Liu, M. Fang, Z. Huang, T. B. Sercombe, A selective laser melting and solution heat treatment refined Al–12Si alloy with a controllable ultrafine eutectic microstructure and 25% tensile ductility, Acta Mater. 95 (2015) 74-82.
[7] K. Saeidi, X. Gao, Y. Zhong, Z. J. Shen, Hardened austenite steel with columnar sub-grain structure formed by laser melting, Mater. Sci. Eng. A 625 (2015) 221-229.
[8] X. Lei, L. Dong, Z. Zhang, Y. Liu, Y. Hao, R. Yang, L.-C. Zhang, Microstructure, Texture Evolution and Mechanical Properties of VT3-1 Titanium Alloy Processed by Multi-Pass Drawing and Subsequent Isothermal Annealing, Metals. 7 (2017) 131.
[9] K. Lu, N. Hansen, Structural refinement and deformation mechanisms in nanostructured metals, Scripta Mater. 60 (2009) 1033-1038.
[10] K. Lu, Stabilizing nanostructures in metals using grain and twin boundary architectures, Nat. Rev. Mater. 1 (2016) 16019.
[11] K. Lu, L. Lu, S. Suresh, Strengthening materials by engineering coherent internal boundaries at the nanoscale, Science 324 (2009) 349-352.
[12] G. Yu, D. Gu, D. Dai, M. Xia, C. Ma, K. Chang, Influence of processing parameters on laser penetration depth and melting/re-melting densification during selective laser melting of aluminum alloy, Appl. Phys. A 122 (2016) 891.
[13] P. Delroisse, O. Rigo, P. Jacques, A. Simar, AlSi10Mg lattice structures processed by selective laser melting: influence of the geometry and the heat treatments on the microstructure, TMS (2017)
[14] W. Li, S. Li, J. Liu, A. Zhang, Y. Zhou, Q. Wei, C. Yan, Y. Shi, Effect of heat treatment on AlSi10Mg alloy fabricated by selective laser melting: Microstructure evolution, mechanical properties and fracture mechanism, Mater. Sci. Eng., A. 663 (2016) 116-125.
[15] F. Trevisan, F. Calignano, M. Lorusso, J. Pakkanen, A. Aversa, E. P. Ambrosio, M. Lombardi, P. Fino, D. Manfredi, On the Selective Laser Melting (SLM) of the AlSi10Mg Alloy: Process, Microstructure, and Mechanical Properties, Materials. 10

(2017) 76.
[16] M. Tang, P. C. Pistorius, S. Narra, J. L. Beuth, Rapid solidification: selective laser melting of AlSi10Mg, JOM 68 (2016) 960-966.
[17] G. Sha, H. Möller, W. E. Stumpf, J. Xia, G. Govender, S. Ringer, Solute nanostructures and their strengthening effects in Al–7Si–0.6 Mg alloy F357, Acta Mater. 60 (2012) 692-701.
[18] A. B. Anwar, Q.-C. Pham, Selective laser melting of AlSi10Mg: Effects of scan direction, part placement and inert gas flow velocity on tensile strength, J Mater Process Tech. 240 (2017) 388-396.
[19] H. Rao, S. Giet, K. Yang, X. Wu, C. H. Davies, The influence of processing parameters on aluminium alloy A357 manufactured by Selective Laser Melting, Materials and Design. 109 (2016) 334-346.
[20] T. Kimura, T. Nakamoto, Microstructures and mechanical properties of A356 (AlSi7Mg0.3) aluminum alloy fabricated by selective laser melting, Mater. Des. 89 (2016) 1294-1301.
[21] J.-P. Kruth, L. Froyen, J. Van Vaerenbergh, P. Mercelis, M. Rombouts, B. Lauwers, Selective laser melting of iron-based powder, J Mater Process Tech. 149 (2004) 616-622.
[22] K. Lu, Making strong nanomaterials ductile with gradients, Science. 345 (2014) 1455-1456.
[23] S. D. McDonald, K. Nogita, A. K. Dahle, Eutectic nucleation in Al–Si alloys, Acta Mater. 52 (2004) 4273-4280.
[24] J. Delahaye, O. Rigo, J. Lecomte-Beckers, A. Habraken, A. Mertens, Influence of Si precipitates on fracture mechanisms of AlSi10Mg parts processed by Selective Laser Melting, (2017)
[25] A. Mazahery, M. O. Shabani, Modification mechanism and microstructural characteristics of eutectic Si in casting Al-Si alloys: A review on experimental and numerical studies, JOM. 66 (2014) 726-738.
[26] L. Lu, K. Nogita, A. Dahle, Combining Sr and Na additions in hypoeutectic Al–Si foundry alloys, Mater. Sci. Eng., A. 399 (2005) 244-253.
[27] S. Bose, R. Kumar, Structure of rapidly solidified aluminium-silicon alloys, J. Mater. Sci. 8 (1973) 1795-1799.
[28] M. Cabrini, S. Lorenzi, T. Pastore, S. Pellegrini, M. Pavese, P. Fino, E. P. Ambrosio, F. Calignano, D. Manfredi, Corrosion resistance of direct metal laser sintering AlSiMg alloy, Surf. Interface Anal. 48 (2016) 818-826.
[29] G. Dinda, A. Dasgupta, J. Mazumder, Texture control during laser deposition of nickel-based superalloy, Scripta Mater. 67 (2012) 503-506.
[30] R. A. Donald, P. P. Pradeep, D. K. Bhattacharya, Essentials of materials science and engineering Thomson Pubication, 2004.
[31] E. Brandl, U. Heckenberger, V. Holzinger, D. Buchbinder, Additive manufactured AlSi10Mg samples using Selective Laser Melting (SLM): Microstructure, high cycle fatigue, and fracture behavior, Materials and Design. 34 (2012) 159-169.
[32] X. Wang, L.-C. Zhang, M. Fang, T. B. Sercombe, The effect of atmosphere on the structure and properties of a selective laser melted Al–12Si alloy, Mater. Sci. Eng.,

A. 597 (2014) 370-375.
[33] G. Roy, J. Elmer, T. DebRoy, Mathematical modeling of heat transfer, fluid flow, and solidification during linear welding with a pulsed laser beam, J. Appl. Phys. 100 (2006) 034903.
[34] D. S. Yong, Y. C. Li, N. S. Chang, P. J. Campagnola, S. J. Chen, Fabrication of three-dimensional multi-protein microstructures for cell migration and adhesion enhancement, Biomed Opt Express. 6 (2015) 480-490.
[35] D. Adebiyi, A. Popoola, Mitigation of abrasive wear damage of Ti–6Al–4V by laser surface alloying, Materials and Design. 74 (2015) 67-75.
[36] P. Nagpal, I. Baker, Effect of cooling rate on hardness of FeAl and NiAl, Metall. Trans. A. 21 (1990) 2281-2282.
[37] L. Murr, K. Amato, S. Li, Y. Tian, X. Cheng, S. Gaytan, E. Martinez, P. Shindo, F. Medina, R. Wicker, Microstructure and mechanical properties of open-cellular biomaterials prototypes for total knee replacement implants fabricated by electron beam melting, J Mech Behav Biomed Mater. 4 (2011) 1396-1411.
[38] S. Li, L. Murr, X. Cheng, Z. Zhang, Y. Hao, R. Yang, F. Medina, R. Wicker, Compression fatigue behavior of Ti–6Al–4V mesh arrays fabricated by electron beam melting, Acta Mater. 60 (2012) 793-802.
[39] S. J. Li, Q. S. Xu, Z. Wang, W. T. Hou, Y. L. Hao, R. Yang, L. Murr, Influence of cell shape on mechanical properties of Ti–6Al–4V meshes fabricated by electron beam melting method, Acta Biomater. 10 (2014) 4537-4547.
[40] Y. Liu, S. Li, H. Wang, W. Hou, Y. Hao, R. Yang, T. Sercombe, L.-C. Zhang, Microstructure, defects and mechanical behavior of beta-type titanium porous structures manufactured by electron beam melting and selective laser melting, Acta Mater. 113 (2016) 56-67.
[41] X. Zhao, S. Li, M. Zhang, Y. Liu, T. B. Sercombe, S. Wang, Y. Hao, R. Yang, L. E. Murr, Comparison of the microstructures and mechanical properties of Ti–6Al–4V fabricated by selective laser melting and electron beam melting, Mater. Des. 95 (2016) 21-31.
[42] S. Pauly, L. Löber, R. Petters, M. Stoica, S. Scudino, U. Kühn, J. Eckert, Processing metallic glasses by selective laser melting, Mater Today 16 (2013) 37-41.
[43] K. Prashanth, S. Scudino, H. Klauss, K. B. Surreddi, L. Löber, Z. Wang, A. Chaubey, U. Kühn, J. Eckert, Microstructure and mechanical properties of Al–12Si produced by selective laser melting: Effect of heat treatment, Mater. Sci. Eng. A 590 (2014) 153-160.
[44] S. Al-Bermani, M. Blackmore, W. Zhang, I. Todd, The origin of microstructural diversity, texture, and mechanical properties in electron beam melted Ti-6Al-4V, Metall. Mater. Trans. A 41 (2010) 3422-3434.
[45] Y. Liu, X. Li, L.-C. Zhang, T. Sercombe, Processing and properties of topologically optimised biomedical Ti–24Nb–4Zr–8Sn scaffolds manufactured by selective laser melting, Mater. Sci. Eng., A. 642 (2015) 268-278.
[46] Y. Liu, R. Hu, T. Zhang, H. Kou, J. Wang, G. Yang, J. Li, Dendritic Growth and Microstructure Evolution with Different Cooling Rates in Ti48Al2Cr2Nb Alloy, J. Mater. Eng. Perform. 25 (2016) 38-45.

[47] D. Stefanescu, Science and engineering of casting solidification, 2nd ed., Springer, 2009.
[48] P. Hirsch, J. Silcox, R. Smallman, K. Westmacott, Dislocation loops in quenched aluminium, Philos. Mag. 3 (1958) 897-908.
[49] Z. Ma, J. Bi, Y. Lu, H. Shen, Y. Gao, Abrasive wear of discontiuous SiC reinforced aluminum alloy composites, Wear 148 (1991) 287-293.
[50] M. M. Haque, M. Maleque, Effect of process variables on structure and properties of aluminium–silicon piston alloy, J. Mater. Process. Tech. 77 (1998) 122-128.

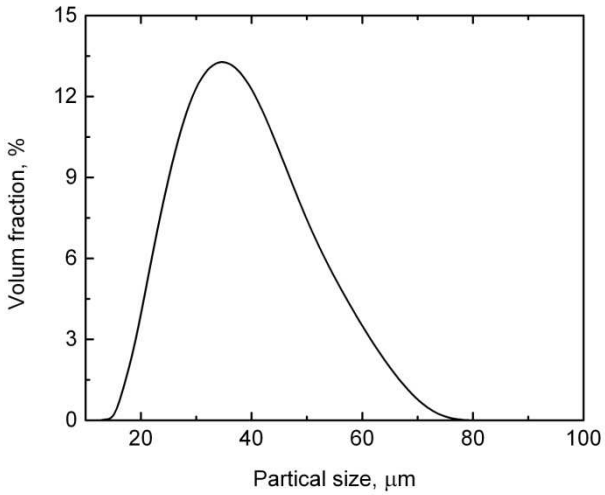

(a)

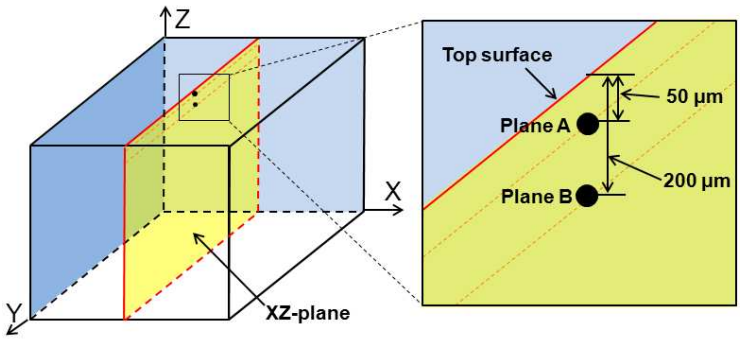

(b)

Fig.1 (a) The size distribution of the powder used, (b) 3D-schematic representation of SLM-produced AlSi10Mg alloy cubic samples with a size of 10 mm × 10 mm × 10 mm and two different studied planes, groups A and B.

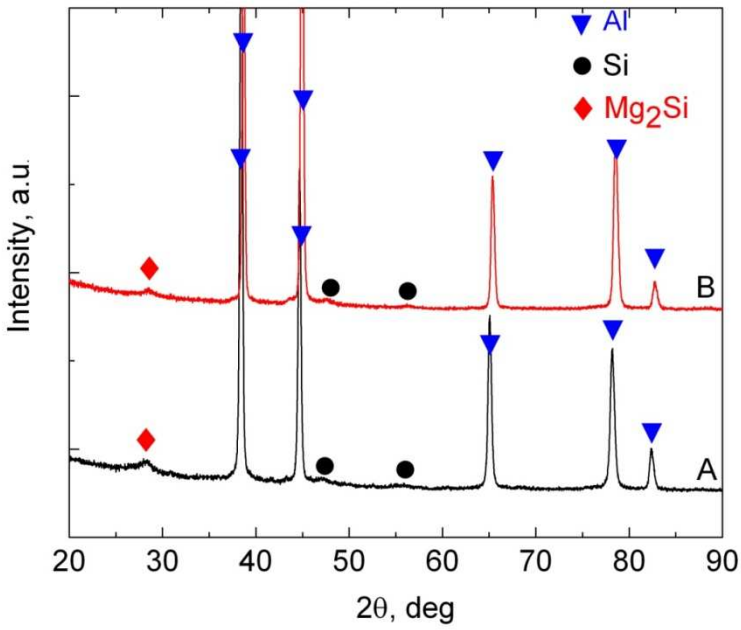

Fig. 2 XRD patterns for the group A and B of the SLM-produced AlSi10Mg alloy

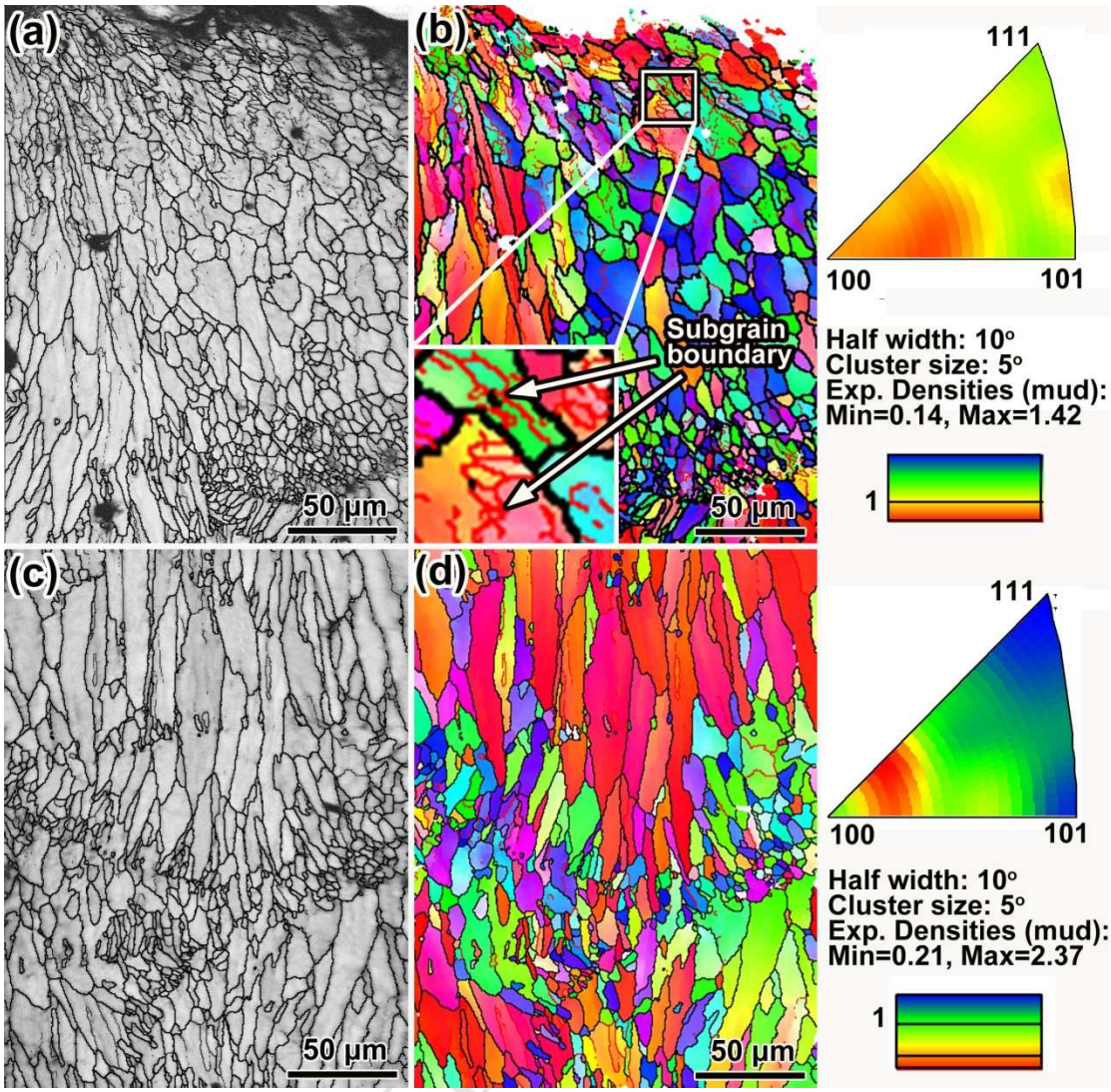

Fig. 3 EBSD image of SLM-produced AlSi10Mg alloy, (a) and (b) are the morphologies of surface area (this area including both groups A and B), where the sub-boundaries are very clearly in red color near the position of group A, but the group B and bottom area ((c) and (d)) have less sub-boundary.

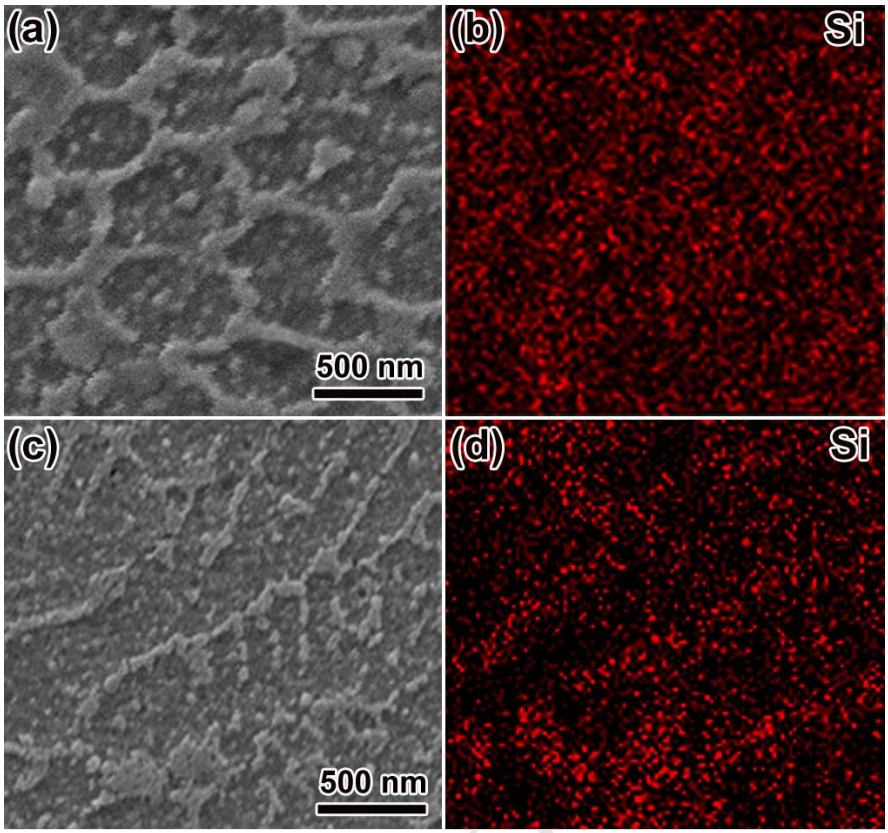

Fig. 4 The SEM-EDS image of of SLM-produced AlSi10Mg at XZ cross-section: (a) and (b) the dendrite morphology and corresponding Si elemental distribution in Sample-A, (c) and (d) the dendrite morphology and corresponding Si elemental distribution in Sample-B.

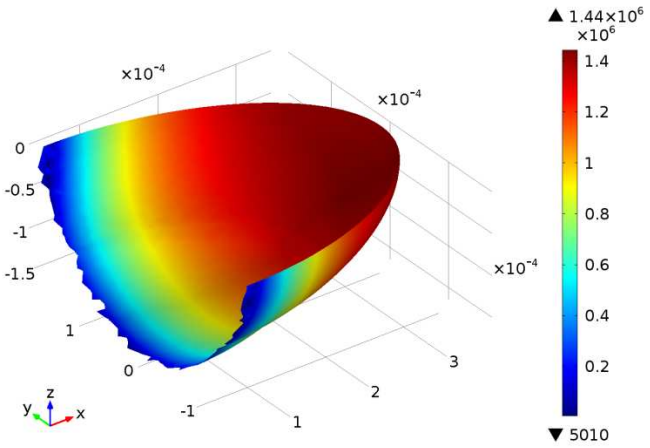

Fig.5 The cooling rate from FEM result of melt boundary.

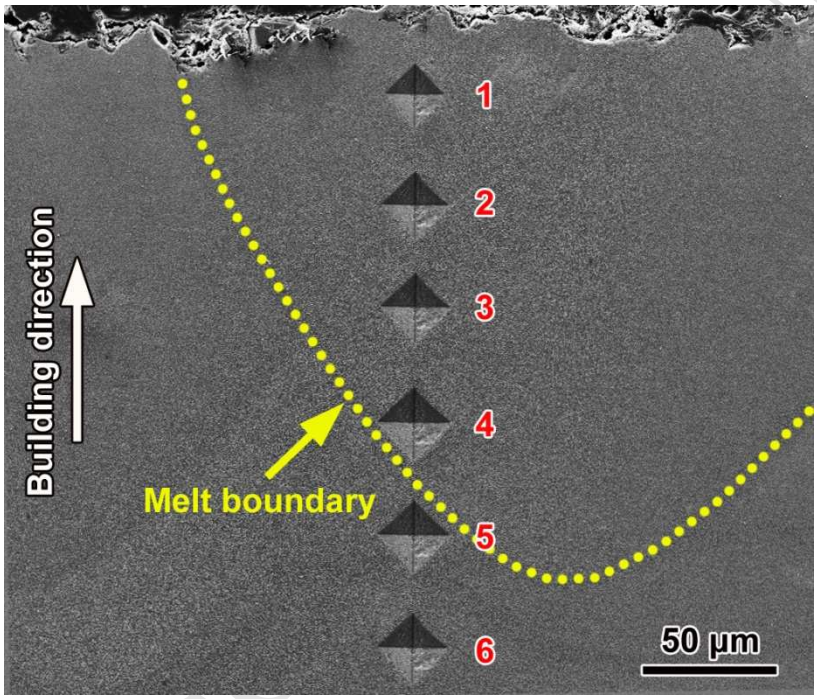

Fig. 6 The SEM image of Vickers hardness measurements from the top surface to inside

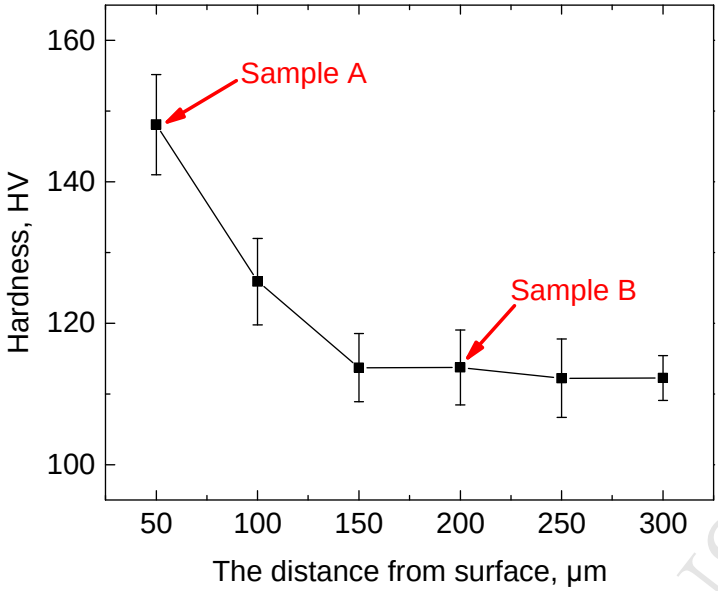

Fig.7 The value of Vickers hardness from the top surface to inside with a distance of 50 μm.

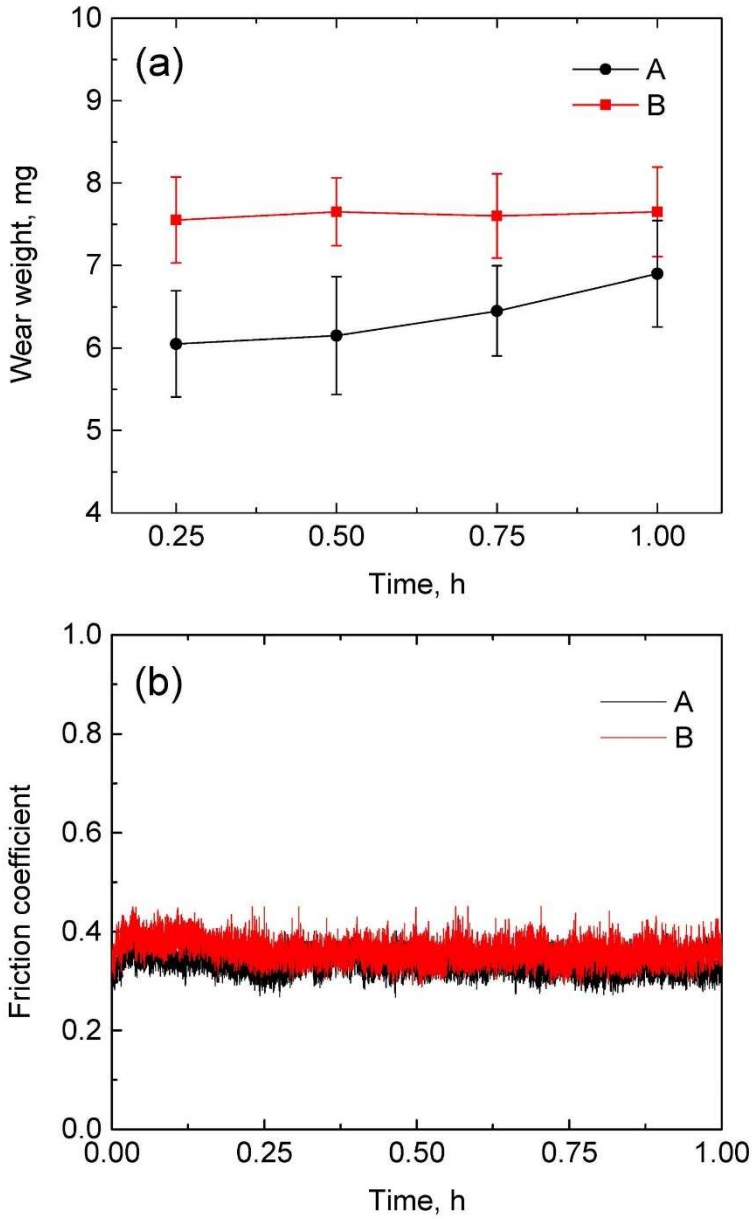

Fig. 8 (a) the relationship of wear rate and time groups A and B, (b) the relationship of coefficient of friction and time groups A and B for AlSi10Mg alloy.

Highlights

- Gradient in microstructure and mechanical property of selective laser melted parts was reported.
- The cooling rate of the melt pool was simulated
- The top surface area has a lower degree of crystallinity of Al matrix than that of core area.
- Obvious massive sub-boundaries and finer dendrites were found in surface area
- The hardness and wear resistance of the surface is better than the core area